All-oxide ferromagnetic resonance and spin pumping with SrIrO_{3}

S. Crossley, A. G. Swartz, K. Nishio, Y. Hikita, and H. Y. Hwang

All-oxide ferromagnetic resonance and spin pumping with SrIrO$_3$

S. Crossley[1,2], A. G. Swartz[1,2], K. Nishio[1,2], Y. Hikita[1,2] and H. Y. Hwang[1,2]

[1] Geballe Laboratory for Advanced Materials, Stanford University, Stanford, California 94305, USA

[2] Stanford Institute for Materials & Energy Sciences, SLAC National Accelerator Laboratory, Menlo Park, California 94025, USA

Abstract

SrIrO$_3$ is a semimetallic complex oxide of interest for spintronic applications due to the large spin-orbit coupling arising from iridium. It has unusual charge transport properties derived from a complex multi-band electronic structure, with electron and hole pockets both contributing to conductivity. We report ferromagnetic resonance of La$_{0.7}$Sr$_{0.3}$MnO$_3$ and SrIrO$_3$ epitaxial bilayer films on (LaAlO$_3$)$_{0.3}$ (Sr$_2$AlTaO$_6$)$_{0.7}$ substrates. Anomalous trends in the out-of-plane magnetic anisotropy and Landé g factor suggest that orbital magnetism is modified by proximity of SrIrO$_3$ at low temperatures, likely contributing to large (~5-fold) enhancements in Gilbert damping. However, enhanced Gilbert damping due to spin pumping is also apparent in the temperature range 250-300 K. The effective spin-mixing conductance is evaluated to be $G^{\text{eff}}_{\uparrow\downarrow} \sim 0.5\times10^{14}\ \Omega^{-1}\ \text{m}^{-2}$, and the spin scattering lengthscale of SrIrO$_3$ is of order ~1 nm. Our work demonstrates the delicate interplay of pure spin current with interfacially mediated spin-orbit effects in a complex oxide heterostructure, exploiting temperature as a control parameter, and should be of interest for both spin pumping and understanding the electronic structure of thin film iridates.

Introduction

Spin-polarized charge currents lie at the heart of commercial devices such as current read heads in magnetic hard drives, but spin transport may also occur in the absence of charge current and its deleterious Joule heating.[1,2] Furthermore, only these 'pure' spin currents can interface the long-lifetime magnon gas that forms in low-damping magnetic insulators and antiferromagnets, with possible applications within novel computational and logic devices.[3-6] There is therefore significant interest in the materials and heterostructures that permit generation of pure spin currents through mechanisms such as spin pumping,[7,2,8,9] spin Hall effects[10,1,11] and the spin Seebeck effect.[12] Within these materials,

the intrinsic spin-orbit coupling is of central importance, as it provides the direct coupling between charge and spin degrees of freedom. Large spin-orbit coupling materials may show a large spin-Hall effect and act as charge current-spin current transducers,[13] whilst insulating small spin-orbit coupling materials may host a high-mobility magnon gas and thus act as macro-scale spin vectors.[14] However, the overall performance of heterostructures for pure spin current devices is also determined by many additional factors, such as the spin transparency of interfaces.

Iridates have attracted interest for the large intrinsic spin-orbit coupling associated with the heavy iridium element.[15,16] The additional presence of strong electron-electron interactions leads to Mott insulating behavior in low-order Ruddleson-Popper strontium iridates such as Sr_2IrO_4 and $Sr_3Ir_2O_7$,[17-19] but not $SrIrO_3$, which is a semimetallic paramagnet, metastable as a bulk material,[20] while readily stabilized in the form of epitaxial thin films on perovskite substrates.[21-24] The combination of metallicity and large spin-orbit coupling readily suggests potential for efficient scattering of pure spin current into charge current.[25] However, utilizing this large spin-charge transduction effect is dependent on efficient injection of pure spin current across interfaces between $SrIrO_3$ and other materials, such as metallic and oxide ferromagnetic films. All-oxide platforms are of particular interest, in order to fully exploit emergent or intrinsic spin-charge-orbit degrees of freedom in systems such as correlated complex perovskites. The electronic properties of these materials are highly tunable through applied electromagnetic or mechanical fields, which could enable novel functionalities.[26] Here, we have investigated ferromagnetic resonance damping of the archetypal ferromagnetic manganite $La_{0.7}Sr_{0.3}MnO_3$ [LSMO], incorporated into thin film heterostructures with $SrIrO_3$ [SIO]. We find that resonance damping is significantly enhanced by SIO at all measurement temperatures from 100-335 K, but that the influence of spin pumping on these data likely lies in competition to that of proximity orbital magnetism.

Experiment

Epitaxial bilayer films of LSMO (lower layer) and SIO (upper layer) were deposited on heated, polished single crystal substrates of (001)-oriented $(LaAlO_3)_{0.3}$ $(Sr_2AlTaO_6)_{0.7}$ [LSAT] (3 mm × 5 mm surface area, 0.5 mm thick). Note that $SrTiO_3$ substrates used in our previous reports of growth of strontium iridates[23] harbor cavity modes at gigahertz frequencies due to the large dielectric constant of $SrTiO_3$, especially at low temperatures, and thus complicate a ferromagnetic resonance study. For pulsed laser deposition of oxide thin films, we used a KrF excimer laser with wavelength of 248 nm

and pulse duration of ~20 ns. Laser pulses were incident at a 45° angle to the surface of the ceramic target, which was oriented opposite to and 50 mm below the surface of the heated substrate. LSMO films were deposited by ablating a ceramic LSMO target with laser pulses of energy fluence ~1.1 J cm^{-2} per pulse, ablation spot area of ~3.8 mm^2 and pulse repetition rate of 5 Hz. The substrate temperature was ~750 °C, chamber pressure was 210 mTorr pure O_2, and the LSMO film growth rate was ~0.02 nm per laser pulse. SIO films were deposited by ablating a ceramic SIO target 50 % enriched with Ir at ~0.9 J cm^{-2} per laser pulse, ablation spot area of ~3.8 mm^2 and pulse repetition rate of 5 Hz. The substrate temperature was ~650 °C, chamber pressure was 50 mTorr pure O_2, and the SIO film growth rate was ~0.004 nm per laser pulse.

An 8 nm-thick SIO film on LSAT was fabricated to permit study of thin film SIO in isolation. A series of bilayer heterostructures of 9 nm-thick LSMO and t nm-thick SIO (0 nm $< t <$ 15 nm) formed the subjects of our ferromagnetic resonance study. Film thickness, growth rate and low roughness were established by X-ray reflectometry (XRR) [(Fig. 1a] (extrapolating a growth rate for the thinnest SIO films). Due to the denser SIO dominating XRR of bilayer films, we did not confirm a 9 nm thickness of LSMO in bilayer films, but measurements on single component LSMO films made both prior to and after the bilayer series was fabricated confirmed that the LSMO growth rate was highly stable. X-ray diffraction confirmed the growth phase and epitaxy (Fig. 1b). The out-of-plane lattice parameter of 9 nm-thick LSMO was 0.395 nm, and that of the 8 nm-thick SIO film was 0.408 nm. Both single component films therefore experienced a compressive epitaxial strain imposed by the LSAT substrate (lattice parameter 0.387 nm). In the case of a bilayer film of 9 nm-thick LSMO and 15 nm-thick SIO, the lattice parameter of the SIO layer was 0.404 nm, evidencing some strain relaxation given the larger 0.408 nm lattice parameter of the 8 nm-thick SIO single component film.

Static magnetic properties of 9 nm-thick LSMO were measured using a superconducting quantum interference device magnetometer (Quantum Design MPMS). Magnetization hysteresis $M(H)$ (M is in-plane magnetization, H is in-plane applied magnetic field) revealed a saturation magnetization $M_S \sim$ 310 kA m^{-1} at $T =$ 300 K (Fig. 2a). Measurements of zero-field magnetization on heating (Fig. 2b) indicates a Curie temperature of ~335 K which was comparable to that from our previous study of ~9 nm-thick LSMO films grown on substrates of LSAT.[27]

To measure the charge transport properties of 8 nm-thick single layer SIO, ohmic electrical contacts were formed by direct Al wirebonds in a four-point van der Pauw geometry. A cryostat (Quantum

Design PPMS) was used to measure resistivity ρ and Hall resistivity R_H as a function of temperature. We observed a flat $\rho(T) \sim 0.5$ mΩ cm (Fig. 3a) similar to that described in previous references [28,22,29,24]. The temperature coefficient of resistivity was positive and thus nominally metallic for temperatures above 50 K. A small upturn in resistivity, observed in our films at temperatures below ~50 K, is commonly observed in this material[28,29,24] and has been discussed in terms of proximity to an exotic correlated insulating state by reference [24]. We measured $R_H \sim -1 \times 10^{-3}$ cm^3 C^{-1} at room temperature and $R_H \sim -3 \times 10^{-3}$ cm^3 C^{-1} at $T = 10$ K, with the most rapid changes occurring near $T = 150$ K (Fig. 3b), echoing data reported by references [28,22]. In addition to transport data acquired for the SIO film, a linear four-probe resistance measurement at room temperature was used to measure the effective resistivity of all LSMO|SIO bilayer films at room temperature (spring-loaded Au-coated pins were used to permit non-destructive electrical contact). Sheet conductance was observed to depend linearly on SIO thickness t (Fig. 3c), confirming that electrical resistivity was well controlled across this heterostructure series.

Ferromagnetic resonance (FMR) properties were studied in the cryostat with a magnetic field H applied out of the plane of the sample ($0 < \mu_0 H < 1.5$ T where μ_0 is the permeability of free space), and a sinusoidal field modulation (amplitude ~0.1 mT and frequency 3.1 kHz). For excitation of FMR at radio frequencies, we used a broadband coplanar waveguide terminated with a coplanar short, and coated with an insulating 10 µm-thick polyimide film (Fig. 4a). Samples were placed film-side-down on top of the coplanar short, a magnetic antinode. When the coplanar waveguide was excited at frequency 8 GHz $< f <$ 20 GHz using a signal generator (power ~16 dBm), the sample experienced an oscillating in-plane magnetic field of frequency f which excited FMR when the out-of-plane applied field H was equal to the out-of-plane resonance field H_0 of LSMO. FMR was detected by monitoring energy absorption I_{FMR} in the coplanar waveguide using a -10 dB directional coupler and microwave diode detector located outside of the cryostat. The 3.1 kHz modulation of H permitted lock-in amplification to enhance sensitivity, yielding a signal proportional to dI_{FMR}/dH which captured a resonance spectra on continuously sweeping H at -1 mT s^{-1} (Fig. 4a). These spectra were fitted with an asymmetric Lorentzian function to obtain H_0 and the half-width at half-maximum linewidth ΔH. Multiple sweeps and fits were performed to obtain H_0 and ΔH at various frequencies and temperatures for each sample.

For each sample and measurement temperature, $H_0(f)$ and $\Delta H(f)$ were obtained from fitting FMR spectra at 1 GHz intervals in f. The $H_0(f)$ data (Fig. 4b) were fitted to the out-of-plane Kittel equation:

$$f = h^{-1}g\mu_B\mu_0(H_0 - M_{eff}) \qquad (1)$$

Where h is the Planck constant, g is the Landé factor, μ_B is the Bohr magneton and M_{eff} is the effective out-of-plane saturation magnetization (M_{eff} is defined as the sum of the static M_S and the out-of-plane magnetic anisotropy field).

The $\Delta H(f)$ data (Fig. 4c) were fitted to the solution of the Landau-Lifshitz-Gilbert equation for FMR damping:

$$\Delta H = \Delta H_0 + h(g\mu_B\mu_0)^{-1}\alpha f \qquad (2)$$

Where ΔH_0 is the inhomogeneous broadening, and α is the dimensionless Gilbert damping coefficient. Contributions to in-plane linewidth from two magnon damping are highly prominent in LSMO thin films,[30,31] and are thought to be enhanced by spin pumping,[30] but are absent from our data due to use of an out-of-plane FMR geometry. Low frequency broadening, due nominally to inhomogeneity of the waveguide impedance in the vicinity of the sample,[31] was apparent in some datasets as a low frequency upturn in $\mu_0\Delta H(f)$ at small values of f. In these cases we selected only higher frequency data for fitting to Equation 2.

Results

The materials parameters M_{eff}, g and α of bilayer films SIO (t nm-thick) | LSMO (9 nm-thick) || LSAT were evaluated as a function of t and temperature T (Fig. 5). At higher temperatures above ~300 K, M_{eff} and g displayed no clear SIO thickness dependence, but displayed a strong temperature dependence as the 335 K Curie temperature was approached. The phase transition was also apparent in $\alpha(T)$ which exhibited high variability above 300 K, such that values in that temperature range should be regarded as only nominal. On reducing temperature below 300 K, a clear divergence of both M_{eff} and g emerged between the bare LSMO film and the bilayer of LSMO with only sub-nm SIO ($t < 1$ nm), and the bilayer films with LSMO and thicker SIO ($t > 1$ nm). In the intermediate temperature range of 200 K< T < 300 K, the values of α were relatively stable but 2-3 times larger for $t > 1$ nm as compared to $t < 1$ nm. At temperatures below ~150 K, the values of α increased steadily for $t < 1$ nm. This increase was also observed for $t > 1$ nm, but was much sharper and had its onset at the higher

temperature of ~200 K. Thus, in the lower temperature range the damping at larger t was enhanced 4-6 fold with respect to that of the LSMO film alone.

Discussion

The structural, static magnetic and charge transport properties of our LSMO and SIO films are similar to those reported by others.[27,28,22,29] The unusual contrast of flat $\rho(T)$ and strongly varying $R_H(T)$ for SIO (Fig. 2) has been discussed by reference [22] with the benefit of angular resolved photoemission spectroscopy. The Hall behavior is attributed to multiband transport where electron conduction becomes increasingly dominant over holes at low temperatures, due to mismatched and varying effective carrier mass.

The dynamic magnetic properties of our LSMO (Fig. 4) are similar to that reported in previous work for the out-of-plane geometry, which suppresses two magnon damping.[30] The room-temperature value of $M_{eff} = 297$ kA m^{-1} (372 mT) is very similar to the measured $M_S = 310$ kA m^{-1} (Fig. 2a), implying a small out-of-plane magneto-crystalline anisotropy (note that this represents only a small perturbation to the overall in-plane anisotropy of our LSMO films, which is determined by demagnetization factors). The low Gilbert damping of 1.4×10^{-3} is similar to previous studies[30-32] and is considerably smaller than the $>6 \times 10^{-3}$ values of prototypical permalloy films.[33] It has been discussed in terms of the half metallicity of LSMO.[34] The increase in damping as temperature is reduced below 150 K could be related to an impurity relaxation mechanism proposed for Garnet films[35].

To understand the dynamic magnetic behavior of our bilayer films of LSMO and t nm-thick SIO, we consider the spin pumping model.[7,2,8] Spin pumping leads to higher damping because the reservoir of dynamic angular momentum in the resonant LSMO film effectively gets drained by outward spin current into the SIO. The pure spin current flows into an admittance (interfacial and relating to SIO) parameterized by the effective spin-mixing conductance $G^{eff}_{\uparrow\downarrow}$ which is proportional to the damping enhancement $\Delta\alpha$ as follows:

$$G^{eff}_{\uparrow\downarrow} = [2e^2/h]2\pi M_S t_{LSMO}(g\mu_B)^{-1}\Delta\alpha \qquad (3)$$

Where $[2e^2/h]$ is the conductance quantum (omitted if evaluating $G^{eff}_{\uparrow\downarrow}$ in units of m^{-2}), and $t_{LSMO} = 9$ nm. However, the spin current model is applicable only if the overall ferromagnetic

properties of the bilayer have not been modified through a proximity or interface effect from the adjacent high spin-orbit coupling SIO. This condition is challenging to prove, but an important indicator is provided by the magnetic anisotropy and particularly the Landé factor, whose variations can represent proxies for the admixture of orbital magnetism within LSMO. A further caveat with the spin pumping model is the role of possible interfacial spin memory loss effects (observed for example, in Co-Pt bilayers), where the spin current becomes depolarized.[36] Finally, we note a report of an important role for radiation losses in low-damping $Y_3Fe_5O_{12}$-Pt bilayers, due to eddy currents induced in the platinum which plays the equivalent role of our SIO.[37] In metallic systems these two complicating phenomena can be controlled for by introducing a highly spin-transparent spacer material, but no similar material for this role has been established for perovskite oxides. However, the spin memory loss effect reported by reference [[36]] required only a 2-fold correction to $G^{eff}_{\uparrow\downarrow}$, and not an order-of-magnitude. The radiative Gilbert damping of bilayer $Y_3Fe_5O_{12}$-Pt reported in reference [[37]] was more than an order-of-magnitude smaller than the overall damping of our LSMO-SIO bilayers. Furthermore, the addition of conductive Pt to insulating $Y_3Fe_5O_{12}$ effectively 'switches on' radiation damping that was not previously present. This is not the situation for LSMO and SIO, which display comparable conductivities at room temperature (Fig. 3c).

The temperature dependence of M_{eff} (Fig. 5a) and g (Fig. 5b) reflects increasingly divergent behavior in the overall bilayer magnetism, as SIO is added ($t > 1$ nm) and temperature is lowered ($T < 250$ K). It therefore seems quite plausible that much of the large $\Delta\alpha \sim 4\times10^{-3}$ at low temperatures (Fig. 5c) is related to changes in the effective orbital magnetism of the bilayer, induced by the proximity of SIO. It is safer to apply the spin pumping model in the higher temperature range of $250 \leq T \leq 300$ K, where highly anomalous behavior in M_{eff} and g are not observed, and the temperature dependence of Gilbert damping is more stable. Invocation of Equation 3 with data in this temperature range using mean values of $M_S \sim M_{eff} = 342$ kA m^{-1} and $\Delta\alpha \sim 0.6\times10^{-3}$ yields $G^{eff}_{\uparrow\downarrow} \sim 0.5\times10^{14}$ Ω^{-1} m^{-2} for the LSMO-SIO interface, which is smaller than values reported for LSMO-$SrRuO_3$,[30] but of a comparable order-of-magnitude. Furthermore, the absence of an apparent gradual enhancement in $\Delta\alpha$ as a function of increasing t indicates a short spin scattering lengthscale for SIO of order ~1 nm. This value, comparable to Pt and $SrRuO_3$, is quite reasonable given the very large spin-orbit coupling of SIO, and harbors some promise of a large spin Hall ratio, as noted also by others.[25]

The ability of high spin-orbit coupling metals to dramatically modify the magnetic anisotropy of ferromagnetic films has been known for several decades.[38] Initially proposed mechanisms were focused

on misfit strain,[38] but the present consensus incorporates interfacial spin-orbit coupling,[39] a concept that is highly compatible with our observation that g in addition to M_{eff} is influenced by SIO. Additional support for spin-orbit coupling may be inferred from the large reported changes in magnetic anisotropy of LSMO-SIO superlattices.[40] We also note a recent report of exchange-coupled LSMO layers through a SIO interlayer.[41]

Finally, we speculate on a possible link between the large changes in Hall resistance in SIO (Fig. 3b) and the large changes in $\Delta\alpha$ as a function of temperature (Fig. 5c). Proximity-induced orbital magnetism is frequently discussed in terms of 3d-5d orbital hybridization.[40] This is challenging to directly relate to the relative predominance of electron and hole transport, however the band structure changes that drive the observed $R_H(T)$ could originate from the same instabilities that might enhance a magnetic proximity effect. For the case of spin pumping, we note that electrons and holes may not be *a priori* expected to show similar spin transport properties within SIO, or to interact in the same way with the electrons of LSMO at the LSMO-SIO interface. Thus, if the large $\Delta\alpha$ at low temperatures were to be interpreted purely in terms of spin pumping (i.e. overstepping the contrary indications apparent in the behavior of g and M_{eff}), the correlation with enhanced R_H would be quite marked. Further work is required to understand these possible links.

Conclusions

In conclusion, we have measured the ferromagnetic resonance properties of bilayer films of La$_{0.7}$Sr$_{0.3}$MnO$_3$ [LSMO] and SrIrO$_3$ [SIO] on (LaAlO$_3$)$_{0.3}$ (Sr$_2$AlTaO$_6$)$_{0.7}$ [LSAT] substrates. Large changes in magnetic damping are observed, particularly at low temperatures. By taking full consideration of concurrent changes in magnetic anisotropy and the Landé factor, we determine that this is likely due to the concerted effects of spin pumping and proximity orbital magnetism induced by the heavy, high spin-orbit coupling iridium. Our results are promising for SrIrO$_3$ as a spin Hall material for spintronic devices that operate through pure spin currents.

Acknowledgements

Directed Research and Development program at SLAC National Accelerator Laboratory (FMR measurements).

References

[1] M. I. Dyakonov and V. I. Perel. *Phys. Lett.* **35A,** 459 (1971).

[2] Y. Tserkovnyak, A. Brataas and G. E. W. Bauer. *Phys. Rev. Lett.* **88,** 117601 (2002).

[3] D. Sander, S. O. Valenzuela, D. Makarov, C. H. Marrows, E. E. Fullerton, P. Fischer, J. McCord, P. Vavassori, S. Mangin, P. Pirro, B. Hillebrands, A. D. Kent, T. Jungwirth, O. Gutfleisch, C. G. Kim and A. Berger. *J. Phys. D: Appl. Phys*. **50,** 363001 (2017).

[4] A. V. Chumak, V. I. Vasyuchka, A. A. Serga and B. Hillebrands. *Nature Physics* **11,** 453 (2015).

[5] T. Jungwirth, X. Marti, P. Wadley and J. Wunderlich. *Nature Nanotechnology* **11,** 231 (2016).

[6] J. Železný, P. Wadley, K. Olejník, A. Hoffmann and H. Ohno. *Nature Physics* **14,** 220 (2018).

[7] R. Urban, G. Woltersdorf, and B. Heinrich. *Phys. Rev. Lett.* **87,** 217204 (2001).

[8] Y. Tserkovnyak, A. Brataas and G. E. W. Bauer. *Phys. Rev. B* **66,** 224403 (2002).

[9] E. Saitoh, M. Ueda, H. Miyajima and G. Tatara. *Appl. Phys. Lett.* **88,** 182509 (2006).

[10] J. Sinova, S. O. Valenzuela, J. Wunderlich, C. H. Back and T. Jungwirth. *Rev. Mod. Phys.* **87,** 1213 (2015).

[11] Y. K. Kato, R. C. Myers, A. C. Gossard and D. D. Awschalom. *Science* **306,** 1910 (2004).

[12] K. Uchida, S. Takahashi, K. Harii, J. Ieda, W. Koshibae, K. Ando, S. Maekawa and E. Saitoh. *Nature* **455,** 778 (2008).

[13] L. Liu, T. Moriyama, D. C. Ralph, and R. A. Buhrman. *Phys. Rev. Lett.* **106,** 036601 (2011).

[14] Y. Kajiwara, K. Harii, S. Takahashi, J. Ohe, K. Uchida, M. Mizuguchi, H. Umezawa, H. Kawai, K. Ando, K. Takanashi, S. Maekawa and E. Saitoh. *Nature* **464,** 262 (2010).

[15] K. Fujiwara, Y. Fukuma, J. Matsuno, H. Idzuchi, Y. Niimi, Y. Otani and H. Takagi. *Nat. Comm.* **4,** 2893 (2013).

[16] K.A. Modic, T. E. Smidt, I. Kimchi, N. P. Breznay, A. Biffin, S. Choi, R. D. Johnson, R. Coldea, P. Watkins-Curry, G. T. McCandless, J. Y. Chan, F. Gandara, Z. Islam, A. Vishwanath, A. Shekhter, R. D. McDonald and J. G. Analytis. *Nat. Comm.* **5,** 4203 (2014).

[17] B. J. Kim, Hosub Jin, S. J. Moon, J.-Y. Kim, B.-G. Park, C. S. Leem, Jaejun Yu, T. W. Noh, C. Kim, S.-J. Oh, J.-H. Park, V. Durairaj, G. Cao and E. Rotenberg. *Phys. Rev. Lett.* **101,** 076402 (2008).

[18] S. J. Moon, H. Jin, K. W. Kim, W. S. Choi, Y. S. Lee, J. Yu, G. Cao, A. Sumi, H. Funakubo, C. Bernhard, and T. W. Noh. *Phys. Rev. Lett.* **101,** 226402 (2008).

[19] D. Pesin and L. Balents. *Nature Physics* **6,** 376 (2010).

[20] J. M. Longo, J. A. Kafalas and R. J. Arnott. *J. Sol. Stat. Chem.* **3,** 174 (1971).

[21] Y. K. Kim, A. Sumi, K. Takahashi, S. Yokoyama, S. Ito, T. Wanatabe, K. Akiyami, S. Kaneko, K. Saito and H. Funakubo. *Jpn. J. Appl. Phys.* **45,** L36 (2006).

[22] Y. F. Nie, P. D. C. King, C. H. Kim, M. Uchida, H. I. Wei, B. D. Faeth, J. P. Ruf, J. P. C. Ruff, L. Xie, X. Pan, C. J. Fennie, D. G. Schlom, and K. M. Shen. *Phys. Rev. Lett.* **114,** 016401 (2015).

[23] K. Nishio, H. Y. Hwang and Y. Hikita. *APL Materials* **4,** 036102 (2016).

[24] D. J. Groenendijk, C. Autieri, J. Girovsky, M. C. Martinez-Velarte, N. Manca, G. Mattoni, A. M. R. V. L. Monteiro, N. Gauquelin, J. Verbeeck, A. F. Otte, M. Gabay, S. Picozzi, and A. D. Caviglia. *Phys. Rev. Lett.* **119,** 256403 (2017).

[25] A. S. Patri, K. Hwang, H.W. Lee and Y. B. Kim. *Scientific Reports* **8,** 8052 (2018).

[26] H. Y. Hwang, Y. Iwasa, M. Kawasaki, B. Keimer, N. Nagaosa and Y. Tokura. *Nature Materials* **11,** 103 (2012).

[27] B. Kim, D. Kwon, T. Yajima, C. Bell, Y. Hikita, B. G. Kim and H. Y. Hwang. *Appl. Phys. Lett.* **99,** 092513 (2011).

[28] J. Matsuno, K. Ihara, S. Yamamura, H. Wadati, K. Ishii, V. V. Shankar, Hae-Young Kee and H. Takagi. *Phys. Rev. Lett.* **114,** 247209 (2015).

[29] D. J. Groenendijk, N. Manca, G. Mattoni, L. Kootstra, S. Gariglio, Y. Huang, E. van Heumen, and A. D. Caviglia. *Appl. Phys. Lett.* **109,** 041906 (2016).

[30] S. Emori, U. S. Alaan, M. T. Gray, V. Sluka, Y. Chen, A. D. Kent and Y. Suzuki. *Phys. Rev. B* **94,** 224423 (2016).

[31] H. K. Lee, I. Barsukov, A. G. Swartz, B. Kim, L. Yang, H. Y. Hwang, and I. N. Krivorotov. AIP Advances **6,** 055212 (2016).

[32] M. Wahler, N. Homonnay, T. Richter, A. Müller, C. Eisenschmidt, B. Fuhrmann and G. Schmidt. *Scientific Reports* **6,** 28727 (2016).

[33] Y. Zhao, Q. Song, S.-H. Yang, T. Su, W. Yuan, S. S. P. Parkin, J. Shi and W. Han. *Scientific Reports* **6,** 22890 (2016).

[34] C. Liu, C. K. A. Mewes, M. Chshiev, T. Mewes and W. H. Butler. *Appl. Phys. Lett.* **95,** 022509 (2009).

[35] C. L. Jermain, S. V. Aradhya, N. D. Reynolds, R. A. Buhrman, J. T. Brangham, M. R. Page, P. C. Hammel, F. Y. Yang and D. C. Ralph. *Phys. Rev. B* **95,** 174411 (2017).

[36] J.-C. Rojas-Sánchez, N. Reyren, P. Laczkowski, W. Savero, J.-P. Attané, C. Deranlot, M. Jamet, J.-M. George, L. Vila and H. Jaffrès. *Phys. Rev. Lett.* **112,** 106602 (2014).

[37] M. M. Qaid, T. Richter, A. Müller, C. Hauser, C. Ballani, and G. Schmidt. *Phys. Rev. B* **96,** 184405 (2017).

[38] F. J. A. den Broeder, W. Hoving and P. J. H. Bloemen. *J. Magn. Magn. Mater.* **93,** 562 (1991).

[39] D. Odkhuu, S. H. Rhim, N. Park and S. C. Hong. *Phys. Rev. B* **88,** 184405 (2013).

[40] D. Yi, J. Liu, S.-L. Hsu, L. Zhang, Y. Choi, J.-W. Kim, Z. Chen, J. D. Clarkson, C. R. Serrao, E. Arenholz, P. J. Ryan, H. Xu, R. J. Birgeneau and R. Ramesh. *PNAS* **113,** 6397 (2016).

[41] P. Aleshkevych, K. Dybko, P. Dluzewski, E. Dynowska, L. Gladczuk, K. Lasek and P. Przyslupski. *J. Phys. D: Appl. Phys.* **51,** 385002 (2018).

Figure captions

Figure 1. **(a)** X-ray reflectometry of 8 nm-thick $SrIrO_3$ [SIO] deposited on a (001)-oriented $(LaAlO_3)_{0.3} (Sr_2AlTaO_6)_{0.7}$ [LSAT] substrate. **(b)** X-ray diffraction near the (002) Bragg reflections of single layer and bilayer films deposited on LSAT. Upper curve: 9 nm-thick LSMO. Middle curve: 8 nm-thick SIO. Lower curve: bilayer film of 9 nm-thick $La_{0.7}Sr_{0.3}MnO_3$ [LSMO] (lower layer) and 15 nm-thick SIO (upper layer). Curves are offset for clarity.

Figure 2. **(a)** Magnetization M of a 9 nm-thick LSMO single layer film, on sweeping magnetic field $\mu_0 H$ from ±6 T. **(b)** Remnant (zero field) magnetization of a 9 nm-thick LSMO single layer film on sweeping temperature T.

Figure 3. **(a)** Resistivity ρ as a function of temperature for an 8 nm-thick SIO single layer. **(b)** Hall resistance R_H as a function of temperature for the same sample as (a). To obtain these data, magnetic field was swept in ±7 T and the measured Hall voltage was observed to be linear in field. **(c)** Room temperature sheet conductance $\kappa_\square$ as a function of t, for bilayer samples of 9 nm-thick LSMO and t nm-thick SIO.

Figure 4. Ferromagnetic resonance (FMR) of 9 nm-thick LSMO. Red curves are fits to data (black). **(a)** Data show measured field dependence of FMR absorption at a frequency $f = 10$ GHz. Due to the use of field modulation, the observed curve represents the field-derivative of the physical resonance, and is fit with an asymmetric Lorentzian function to extract center H_0 and linewidth ΔH. The out-of-plane

measurement geometry is indicated in the diagram showing the orientation of magnetic field H with respect to the coplanar waveguide (CPW). **(b)** Resonance center $H_0(f)$ is captured by a linear fit whose slope allows the Lande g factor to be determined, and intercept is equal to the effective saturation magnetization M_{eff}. **(c)** Resonance linewidth $\Delta H(f)$ is captured by a linear fit whose slope is proportional to the Gilbert damping parameter α.

Figure 5. Results from fitting data from FMR measurements for bilayer samples of 9 nm-thick LSMO and t nm-thick SIO. We show **(a)** effective saturation magnetization, **(b)** Lande g factor and **(c)** Gilbert damping as a function of temperature.
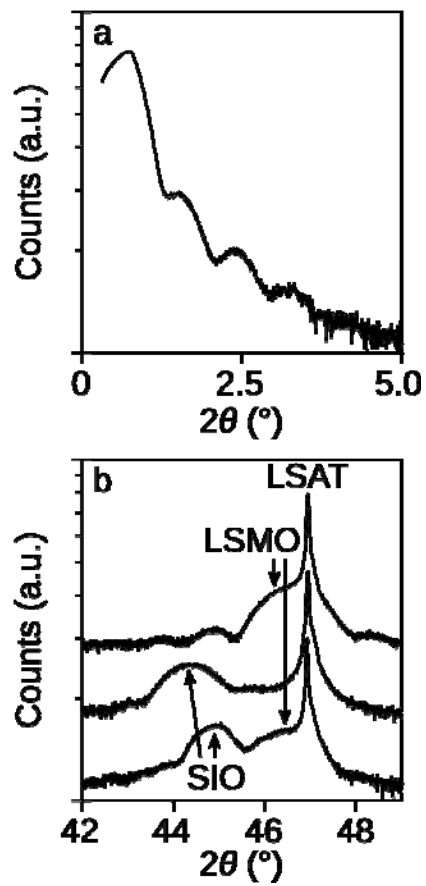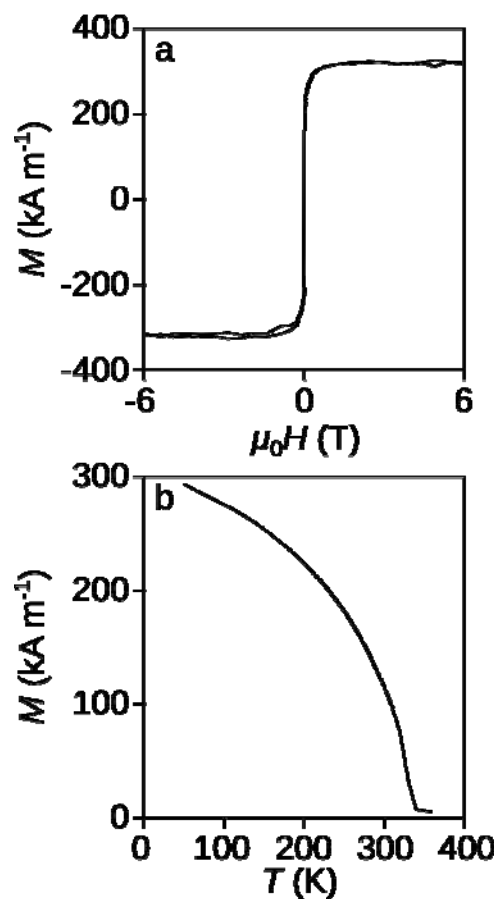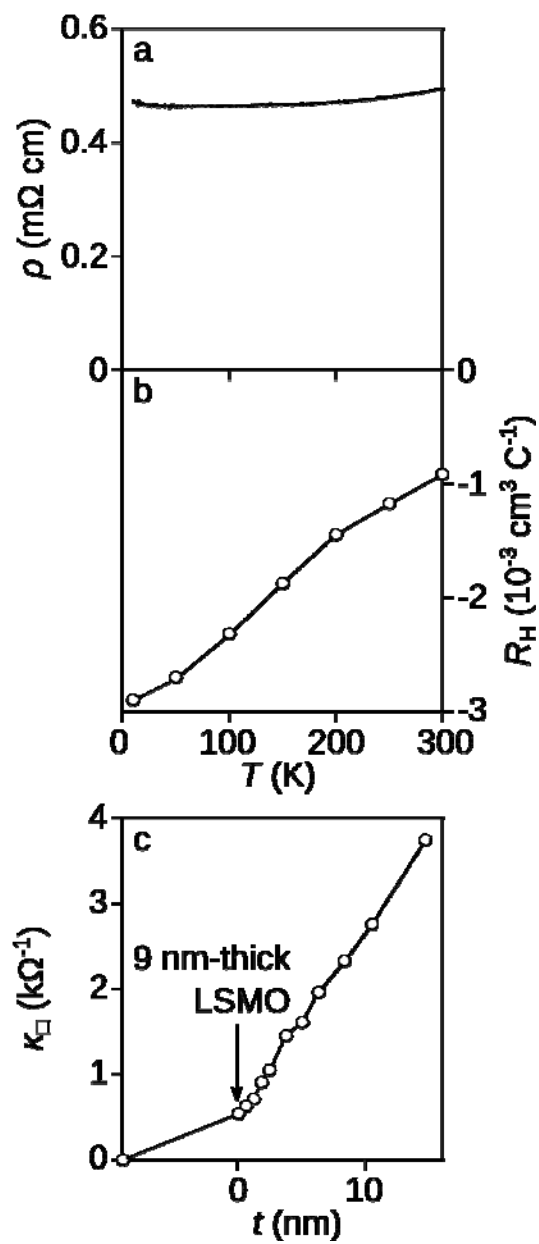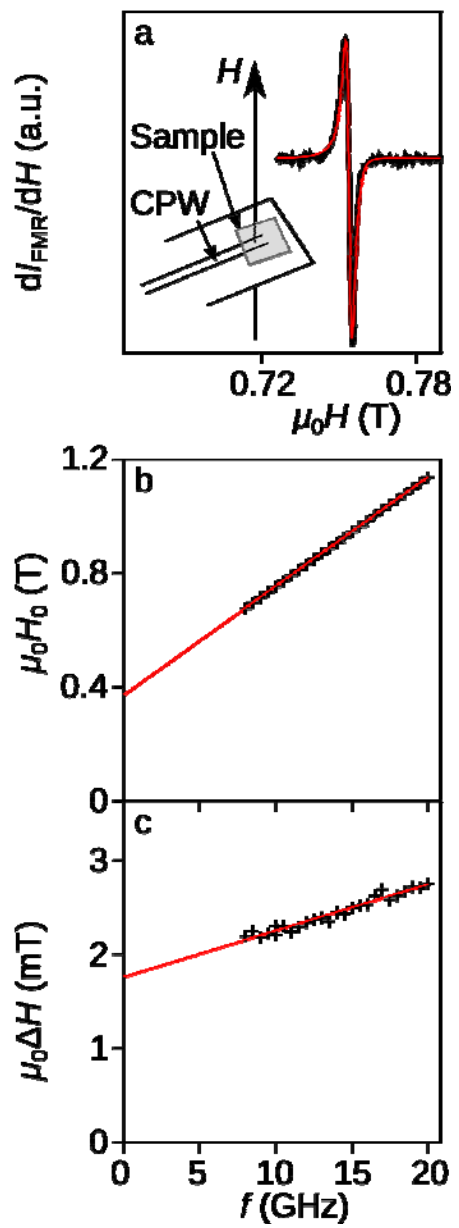
Figure 1

Figure 2

Figure 3

Figure 4

Figure 5